Subsurface granular flow in rotating tumblers: A detailed computational study

Pengfei Chen,[1] Julio M. Ottino,[1,2] and Richard M. Lueptow[2,*]
[1]*Department of Chemical and Biological Engineering, Northwestern University, Evanston, Illinois 60208, USA*
[2]*Department of Mechanical Engineering, Northwestern University, Evanston, Illinois 60208, USA*
(Received 9 April 2008; published 14 August 2008)

To better understand the subsurface velocity field and flowing layer structure, we have performed a detailed numerical study using the discrete element method for the flow of monodisperse particles in half-full three-dimensional (3D) and quasi-2D rotating tumblers. Consistent with prior measurements at the surface, a region of high speed flow with axial components of velocity occurs near each endwall in long tumblers. This region can be eliminated by computationally omitting the friction at the endwalls, confirming that a mass balance argument based on the slowing of particles immediately adjacent to the frictional endwalls explains this phenomenon. The high speed region with the associated axial flow near frictional endwalls persists through the depth of the flowing layer, though the regions of high velocity shift in position and the velocity is lower compared to the surface. The axial flow near the endwalls is localized and independent with the length of the tumbler for tumblers longer than one tumbler diameter, but these regions interact for shorter tumblers. In quasi-2D tumblers, the high speed regions near the endwalls merge resulting in a higher velocity than occurs in a long tumbler, but with a flowing layer that is not as deep. Velocity fluctuations are altered near the endwalls. Particle velocity fluctuations are greatest just below the surface and diminish through the depth of the flowing layer.

DOI: 10.1103/PhysRevE.78.021303 PACS number(s): 45.70.−n, 47.57.Gc

I. INTRODUCTION

The horizontal cylindrical rotating tumbler is a canonical system often used to study the thin flowing surface layer typical of flowing granular materials. Although granular flow has been much studied in recent years [1–3], it is quite difficult to experimentally probe the nature of the flow beneath the visible surface due to the opacity of the particles. To overcome this problem, many researchers have made measurements of the flow in quasi-two-dimensional (quasi-2D) systems [4–10], where the axial dimension of the system is only a few particle diameters in length. Although using a quasi-2D tumbler with transparent endwalls allows the easy measurement of several properties of granular flow including profiles of the velocity and particle number density through the depth of the flowing layer, recent studies have shown that the flow near the middle of the length of the long tumblers is significantly different from that near the endwalls due to friction. Not only is the streamwise velocity near the endwall slower than that at the center of the tumbler [11], but the velocity in quasi-2D tumblers is as much as two times higher than for long tumblers [12]. Furthermore, the streamwise velocity in a long tumbler varies along the length of the tumbler, with a higher velocity in a region adjacent to the endwalls than at the center of the tumbler [12,13]. Thus, it is clear that measurements of the velocity field in a quasi-2D system, while helpful in understanding certain aspects of the flow, do not exactly represent the flow in a "slice" of a long tumbler.

Moreover, the endwall boundary affects the mixing of monodisperse particles [14] and plays a role in initializing axial segregation bands of bidisperse particles [15–17] near the endwall regions. Santomaso *et al.* [14] suggested that there exists an axial flow near the endwalls of rotating tumblers causing the axial mass transport between transverse slices in that region. This axial flow has been confirmed based on measurements of the velocity on the surface of the flowing layer [12] and is corroborated in this study.

The opacity of the particles makes optical techniques for measuring the velocity field below the surface of a granular flow difficult. There are several experimental techniques that can be used to overcome the opacity: fiber-optic probes [18] provide flow measurements at a single point, but the probe disturbs the flow locally; positron emission particle tracking (PEPT) [19] provides measurements deep in the flowing layer, but it is possible to track only one or two particles, not the entire flow field; magnetic resonance imaging (MRI), which requires very expensive equipment, has been used to measure the flow field below the surface in granular systems [11,20,21], but its low spatial and temporal resolution makes it difficult have confidence that it can capture subtle properties of granular flow, such as the axial velocity.

Numerical simulation offers an attractive alternative to experiments that overcomes the problem of using optically based measurement techniques in quasi-2D tumblers and the difficulty of using cumbersome experimental techniques such as MRI and PEPT in long tumblers. Here we present a detailed numerical study of granular flow in rotating cylindrical tumblers using particle dynamics for granular materials, also known as the discrete element method (DEM) [22–24]. Our goal is to provide a detailed and complete examination of the entire three-dimensional flow field throughout the depth of the flowing layer in order to understand the differences between the flow in long tumblers and quasi-2D tumblers. We pay particular attention to the axial flow generated from the frictional endwalls, which is helpful to understand the mechanisms of mixing and segregation near the endwall regions. Using particle dynamics simulations not

*r-lueptow@northwestern.edu

only has the advantage of allowing the examination of the flow structure beneath the free surface, it also permits the investigation of the dependence of the flow on parameters that are not easily controlled in experiments.

II. NUMERICAL METHOD

The discrete element method uses an explicit, constant time step to integrate Newton's second law to describe the translational and rotational motion of individual "soft" particles. The linear-spring dashpot force model [22–24] is used to calculate the normal force between two contacting particles, which consists of two parts: normal elastic spring force and normal viscous damping force $\mathbf{F}_{ij}^n=[k_n\alpha - 2\gamma_n m_{\text{eff}}(\mathbf{V}_{ij}\cdot\hat{\mathbf{r}}_{ij})]\hat{\mathbf{r}}_{ij}$. Here α and $\mathbf{V}_{ij}$ denote the overlap and relative velocity $(\mathbf{V}_i-\mathbf{V}_j)$ of two contacting particles i and j. $\hat{\mathbf{r}}_{ij}$ represents the unit vector in the direction between particles i and j, and $m_{\text{eff}}=\frac{m_i m_j}{m_i+m_j}$ is the reduced mass of these two particles. k_n and γ_n characterize the stiffness and damping of the granular materials and are related to the collision time Δt and restitution coefficient e by $\gamma_n=-\frac{\ln e}{\Delta t}$ and $k_n=[(\frac{\pi}{\Delta t})^2+\gamma_n^2]m_{\text{eff}}$ [23]. For the tangential force, a linear spring at the contact point between two particles provides a restoring force. If this restoring force is larger than the Coulomb frictional force, the spring is "cut" and the force is sliding friction based on Coulomb's law: $\mathbf{F}_{ij}^s=-\min(|k_s\beta|,|\mu\mathbf{F}_{ij}^n|)\text{sgn}(\beta)\hat{\mathbf{s}}$. Here the tangential displacement β is given by $\beta(t)=\int_{t_0}^t \mathbf{V}_{ij}^s dt$, where t_0 is the initial contact time between two particles and $\mathbf{V}_{ij}^s$ is the relative tangential velocity of two particles [25]. The tangential stiffness is $k_s=\frac{2}{7}k_n$ [24]. The velocity-Verlet algorithm [23,26] is used to update the positions and velocities of particles.

We simulate tumblers that are half filled with granular particles and rotating at a speed such that the continuously flowing layer is nearly flat. To avoid the close-packed crystal structure, the particles have a normal size distribution with a variance of $(0.1d)^2$, where d is the mean size of particles (except where noted, we use $d=1.5$ mm in our simulations). The number of particles in the simulation was as many as 110 000, depending on the tumbler dimension and particle size. The parameters of simulation are as follows: tumbler diameter is $D=2R=0.07$ m; the length of the tumbler is varied from $L=0.01$ m to $L=0.15$ m; gravitational acceleration is $g=9.8$ m/s^2; particle properties are for spherical vitamin-E particles (density $\rho=1100$ kg/m^3, restitution coefficient $e=0.89$ [23]) to allow comparison of our simulations with MRI experiments [11] where spherical particles containing liquid cores were used. The only adjustable parameters in the model are the coefficients of friction and the collision time. To achieve the best match with MRI experiments [11], the friction coefficients among particles and between particles and walls are set to $\mu=0.6$; in order to save computer time, the collision time is $\Delta t=1.0\times10^{-4}$ s, which is realistic since the maximum overlap between particles is only a very small fraction of the sum of their radii [27,28]. The integration time step is $dt=\Delta t/40=2.5\times10^{-6}$ s to meet the requirement of numerical stability [23]; the rotational speed is $\omega=3.4$ radians/s, consistent with the experiments [11]. The curved cylindrical wall of the tumbler is modeled using wall particles with properties similar to the mobile particles to prevent the slip along the wall. Geometrically smooth surfaces are used to represent the two endwalls, which are assumed to have infinite mass and radius for the calculation of the collision force between mobile granular particles and the endwalls. The coordinate system sets the origin at the center of the tumbler with the x axis along the streamwise direction, the y axis normal to the free surface, and the z axis along the tumbler axis, as shown in Fig. 1.

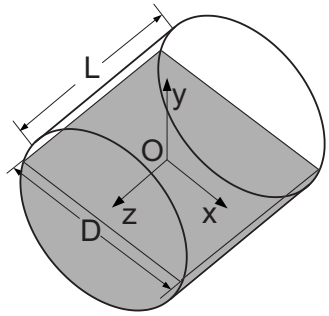

FIG. 1. Coordinate system used in this paper for a 50% full tumbler of granular material.

For analysis of the results, the computational domain is divided into bins (20 bins in each dimension). All local flow properties are obtained by averaging values for all particles within each bin. Although the flow is steady, inherent fluctuations necessitate a long time averaging (typically over one million timesteps) to minimize the standard deviation.

Using MRI, Maneval *et al.* [11] recently measured the streamwise velocity profile experimentally at the midpoint of the flowing layer ($x=0$) for two axial positions: near the end wall and at the center of the tumbler. They tumbled 3 mm particles having a liquid core in a half-filled cylindrical tumbler (0.07 m diameter and 0.06 m axial length, so $L/d=20$) at an angular velocity of 3.4 radians/s, resulting in a continuously flowing, nearly flat flowing layer. The time-averaged velocity profiles over 1.35 tumbler rotations for our particle dynamics simulation for 3 mm particles are plotted against corresponding experimental results in Fig. 2. The primary qualitative characteristics of the velocity profiles are captured by the particle dynamics simulation: the magnitude of the streamwise velocity at different depths, the general nature of the velocity profiles including a nearly linear profile in the flowing layer ($y\geqslant-0.01$ m), a linear profile for the solid body rotation ($y\leqslant-0.02$ m), and the logarithmic transition between these two regions. More importantly, the differences between streamwise velocity profile at the center of the tumbler and near the endwall are well reproduced by the numerical simulation: particles near the endwall are always slower than particles at the same depth in the center of the tumbler. The slight differences between the measured and simulated velocity profiles likely arise from the difficulty in matching the parameters of the simulation (e, Δt, and μ) to the values for the particles in the experiment. The value for e is fixed for vitamin-E particles [23]. The simulation is insensitive to the value for Δt. The only parameter that was adjusted to match the experiments was the frictional coefficient

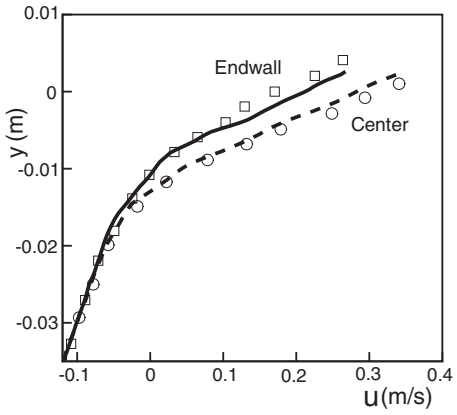

FIG. 2. Comparison of streamwise velocity u(m/s) from particle dynamics simulation (curves) with experimental results (data points) from Maneval *et al.* [11] at the center of the tumbler (○, dashed curve, $z=0$) and near the endwall (□, solid curve, bin adjacent to the endwall).

μ and, in fact, the simulation is relatively insensitive to this as well. Another contact law, the Hertzian normal force law, was also considered, but did not significantly change the results.

Streamtraces obtained by the integration of the local average velocity vector (u and w) for the flow on the free surface ($y=0$) for the case in Fig. 2 are shown in Fig. 3. At the center of the tumbler ($z=0$), the stream traces are straight indicating pure streamwise flow. However, the curved stream traces near the endwalls located at $z=\pm 0.03$ m indicate that particles near the endwalls tend to move toward the center of the tumbler in the upstream part of the flowing layer and then move back toward the endwall in the downstream part. As would be expected, the velocity field is approximately symmetric about the center of the tumbler, $z=0$. These results are consistent with the curved particle trajectories that have been observed in experiments [12]. The results shown in Figs. 2 and 3 indicate that several important details of the actual

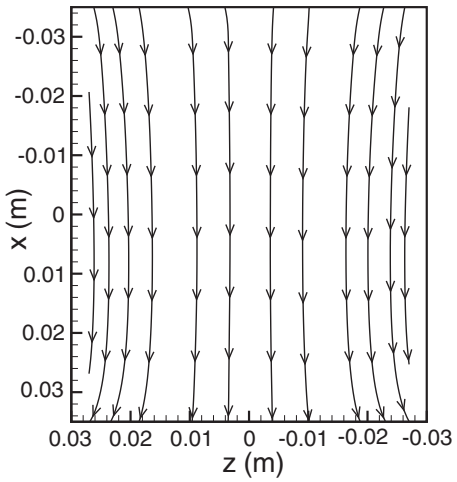

FIG. 3. Streamtraces of the particle flow on the free surface. Flow is from top to bottom. Endwalls are located at $z=\pm 0.03$ m. Curvature of the streamtraces near the endwalls is related to the friction at the endwalls.

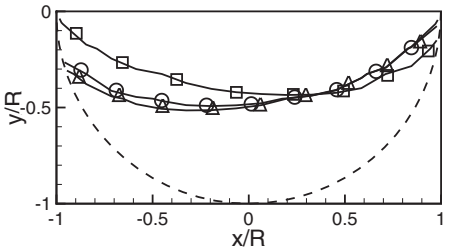

FIG. 4. Boundaries of flowing layer for 1.5 mm particles at $z=0$ m in three tumblers where $y=0$ corresponds to the surface of the flow: △, $L=0.10$ m ($L/D=1.43$); ○, $L=0.05$ m ($L/D=0.71$); and □, $L=0.01$ m ($L/D=0.14$). Flow is from left to right. The dashed curve indicates the tumbler wall.

flow field are captured by DEM simulations. Thus, the particle dynamics technique used here provides an accurate representation of an actual experimental system and provides a solid foundation for the following examination of the subsurface granular flow.

III. RESULTS AND DISCUSSION

The primary objective of this work is to explore the entire flow field in three-dimensional cylindrical tumblers, focusing on the flow beneath the visible surface. We present results for the structure of the flowing layer, streamwise velocity field, velocity fluctuation field, and axial flow field throughout the entire flowing layer. Of particular interest is the impact of the endwalls and the overall tumbler length on the subsurface flow.

A. Flowing layer structure beneath the visible free surface

We consider first the overall structure of the flowing layer. We define the flowing layer as the region in the tumbler where the streamwise velocity in the reference frame of the rotating tumbler is greater than 5% of the surface velocity at the center of the tumbler $[(x,y,z)=(0,0,0)]$, u_0. (This scheme is analogous to that used to define the edge of a boundary layer in fluid flow.) Since the numerical method provides the velocity in the laboratory frame, the solid body rotation of the tumbler is subtracted before identifying the boundary of the flowing layer. As with experiments, a region of creeping motion exists between the freely flowing material and the fixed bed of particles in solid body rotation [10,29].

First, we consider the lower boundary of the flowing layer on the $z=0$ and $x=0$ planes in Figs. 4 and 5 for three cases: a long tumbler with $L=0.10$ m ($L/D=1.43$), a short tumbler with $L=0.05$ m ($L/D=0.71$), and a quasi-2D tumbler with $L=0.01$ m ($L/D=0.14$). To compare them, the streamwise position (x), depth (y) are normalized by the radius (R), and axial position (z) is normalized by the length (L) of the tumbler. In addition, in Fig. 5 the flowing layer depth for a long tumbler where one endwall is frictionless is also shown to illustrate the influence of endwalls on the flowing layer structure. The region above each curve in Figs. 4 and 5 corresponds to the flowing layer and the region below the curve is in near-solid rotation.

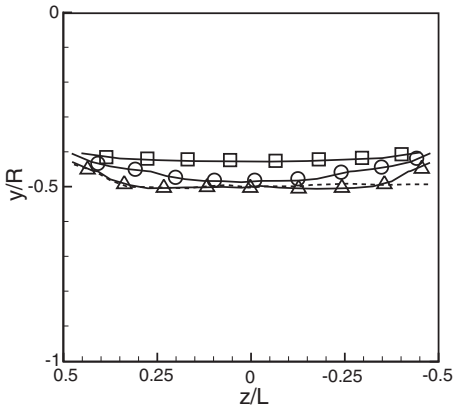

FIG. 5. Boundaries of flowing layer for 1.5 mm particles at $x=0$ m: solid curves indicate three tumblers: △, $L=0.10$ m ($L/D=1.43$); ○, $L=0.05$ m ($L/D=0.71$); and □, $L=0.01$ m ($L/D=0.14$). The dashed curve is for $L=0.10$ m ($L/D=1.43$) with a frictionless right endwall at $z/L=-0.5$.

From Fig. 4, it is clear that at the midlength of the tumbler ($z=0$), the depths of flowing layer at the upstream end of the flow ($x/R=-1$) as the flow is initiated in the long and short tumbler are much larger than that in the quasi-2D tumbler, which means in these two longer tumblers more particles participate the initialization of the inclined flow. More than this, the flowing layers of these three tumblers are not symmetric about the midlength of the flowing layer ($x=0$): the flowing layers in long and short tumblers are skewed to the upstream portion, while the flowing layer of quasi-2D case is skewed to the downstream portion. Clearly, this skewness is related to the geometry of the tumbler. Furthermore, for the first 2/3 of the flowing layer, the depth of the flowing layer in the long tumbler is larger than that in the short tumbler, and both are much larger than that for the quasi-2D tumbler, though both are less for the final 1/3 of the flowing layer.

This difference of the flowing layer depths is also illustrated in Fig. 5, which shows the flowing layer structure along the length of the tumbler at the midlength of the flowing layer ($x=0$). Based on mass conservation, the thinner flowing layer for the quasi-2D tumbler at $x=0$ is consistent with the higher streamwise velocity in the shorter tumblers that has been measured in quasi-2D experiments [12]. Moreover, as shown in Fig. 5, the depth of the flowing layer decreases near the endwalls for all three tumblers, corresponding to the slower streamwise velocity near endwalls shown in Fig. 2. For the two shorter tumblers, the maximum flowing layer depth occurs at the midlength of the tumbler, while for the longer tumbler the maximum depth is around $z/L=\pm 0.2$. Apparently, it is closely related to the high streamwise flow rate at these two positions due to the axial flow near endwalls in the long tumbler, which is discussed in more detail in a later section. This point is validated by the dashed curve of the long tumbler that has a frictionless endwall at $z/L=-0.5$. The flowing layer depth in this case is nearly constant from the frictionless wall to the midlength of the tumbler but overlaps the depth profile for the case when both endwalls have friction for $0 \leqslant z/L \leqslant 0.5$. This clearly demonstrates that the decreased depth of the flowing layer near the endwalls and the two regions where the flowing layer is deeper in the long tumbler ($z/L=\pm 0.2$) result from the frictional interactions between particles and the endwalls. Furthermore, the effects of the two endwalls on flowing structure are independent of each other.

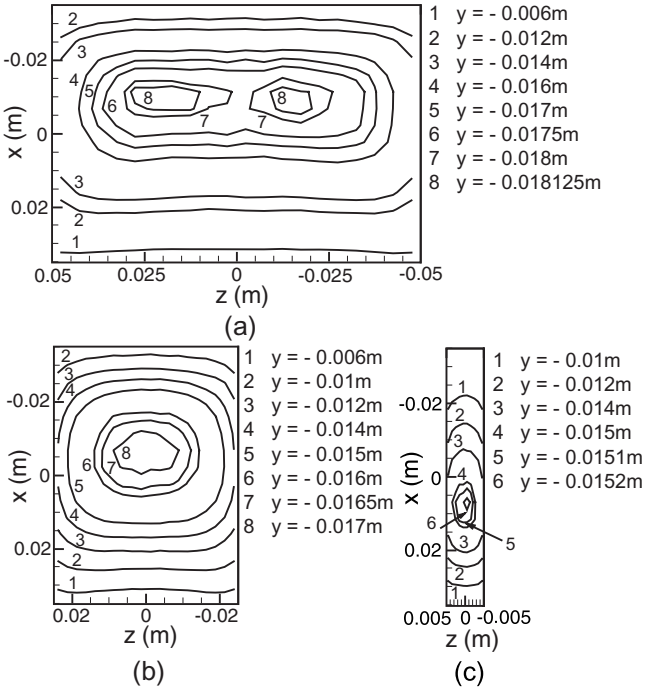

FIG. 6. Flowing layer structure for 1.5 mm particles at different depths for three tumblers shows how the length of the tumbler affects the depth of the flowing layer: (a) $L=0.10$ m ($L/D=1.43$); (b) $L=0.05$ m ($L/D=0.71$); (c) $L=0.01$ m ($L/D=0.14$). Flow is from top to bottom.

An even better comparison of the structure of the flowing layer between the long tumbler and the two shorter tumblers is illustrated in Fig. 6, which shows contours of the flowing layer depth for these three tumblers. For the long tumbler, Fig. 6(a), the flowing layer is deepest at two regions slightly upstream of the axis of rotation. For the short tumbler and quasi-2D tumbler, shown in Figs. 6(b) and 6(c), the tumblers are short enough so that two regions merge into a single region so the flowing layer is deepest at the center of the length of the tumbler. Moreover, consistent with the skewness of the flowing layer shown in Fig. 4, the contours of the flowing layer depth are not symmetric about the axis of rotation of the tumbler at $x=0$ m. The layer is deepest upstream of the tumbler axis for $L=0.10$ and 0.05 m, and downstream for the quasi-2D tumbler. Similar results were obtained for 3 mm particles in the above three tumblers, except that the layer was deepest downstream of the axis of rotation indicating that rheological properties of the particle flow also plays a role in the flowing layer depth.

B. Streamwise velocity field beneath the visible free surface

Closely related to the structure of the flowing layer in the long tumbler, there are two regions of high streamwise velocity, as shown in Fig. 7 for xz planes at different depths from the top surface to near the bottom of the flowing layer.

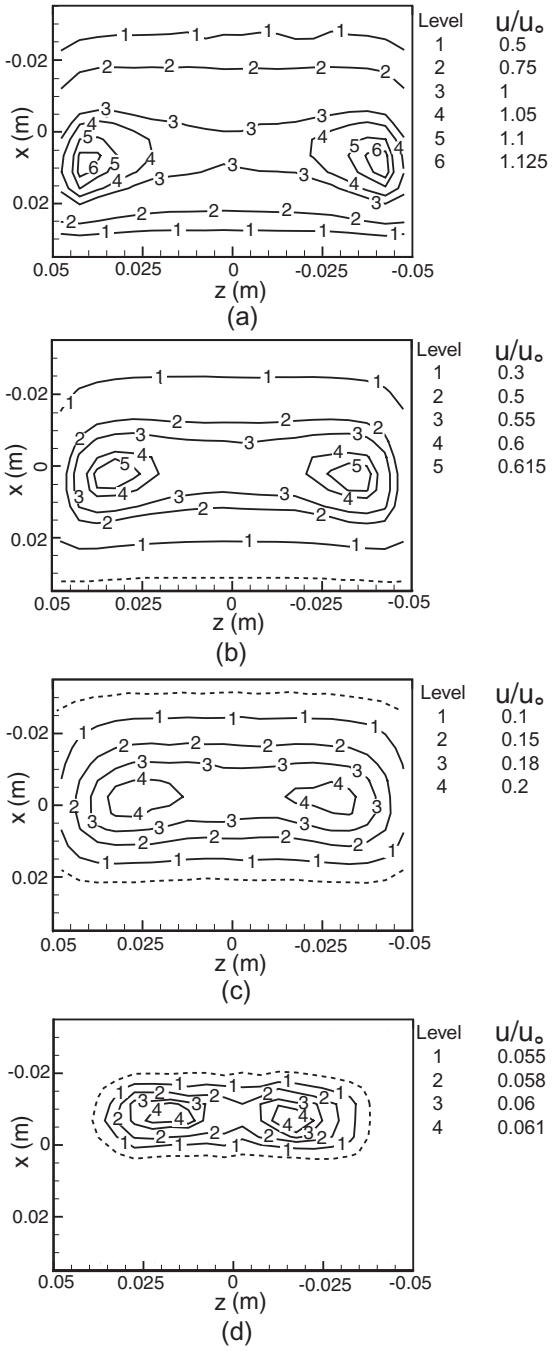

FIG. 7. Contours of streamwise velocity at different depths in the long tumbler of $L=0.10$ m ($L/D=1.43$) for 1.5 mm particles show how the high velocity regions shift position from the surface (a) to deep in the layer (d): (a) $y=0$ m; (b) $y=-0.006$ m; (c) $y=-0.012$ m; (d) $y=-0.017$ m. The dashed contour indicates the edge of the flowing layer at the depth indicated. Flow is from top to bottom.

In Fig. 7, contours of streamwise velocity are plotted after subtracting the solid body rotation and normalizing by the streamwise surface velocity at the center of the tumbler u_0. The dashed curves are the boundaries of flowing layer. It is evident that two high velocity regions exist at the surface and all depths in the flowing layer. The axial positions are always symmetric about the midlength of the tumbler $z=0$ m, consistent with experimental measurements of the surface velocity at $x=0$ [12,13]. However, the position of the two high velocity regions changes with depth in the flowing layer. At the surface, Fig. 7(a), these regions are downstream of the axis of the tumbler, $x=0$ m, and very near the endwall (note that the streamwise velocity in these regions exceeds that at the center of the tumbler at the surface). Moving deeper in the flowing layer these regions shift upstream and away from the endwalls, so that very deep in the flowing layer the high velocity region occurs upstream of the axis of the tumbler [the high velocity regions in Fig. 7(d) are as far as $D/2$ away from the tumbler endwalls]. The locations of the the high velocity regions deep in the layer [Fig. 7(d)] correspond to the deepest portion of the flowing layer [Fig. 6(a)].

Again, keeping one endwall frictionless validates that the friction from endwalls is the origin of these two regions with high streamwise velocity in the long tumbler. Figure 8 shows the streamwise velocity contours for this case at the same four depths as illustrated in Fig. 7. Clearly, no high velocity region exists near the frictionless endwall, and the magnitudes as well as positions of the high velocity regions associated with the frictional endwall are almost identical to those in Fig. 7. It is also clear that the effects of the frictional endwall are negligible throughout the depth of the flowing layer by about $D/2$ from the endwall, consistent with measurements of the surface velocity [12].

Simulations for the short and quasi-2D tumblers show the effect of the interaction between two endwalls on the streamwise velocity field. In Fig. 9, for the short tumbler, there still exist two regions of high streamwise velocity in the upper portion of the flowing layer, but these two regions move toward each other deeper in the layer until they merge at the center of the tumbler at around $y=-0.004$ m, as shown in Fig. 9(b). Below this depth, there is only one region of high streamwise velocity, which occurs at the center of the tumbler [Figs. 9(c) and 9(d)]. For the quasi-2D case, which is shown in Fig. 10, only one region with high streamwise velocity exists throughout the depth of the flowing layer. The streamwise positions of regions of high streamwise velocity for the short and quasi-2D tumbler move upstream with the depth, just as in the long tumbler. However, the high speed region for the quasi-2D case is always downstream of the midlength of the flowing layer unlike the short and long tumblers where it is upstream of the midlength deep in the layer. The locations of the high speed regions deep in the layer for the short and quasi-2D tumblers [Figs. 9(d) and 10(b)] correspond to the deepest portion of the flowing layer [Figs. 6(b) and 6(c)]. The shift in location of the greatest depth downstream as L/D decreases might be attributed to friction at the walls slowing the particles in the highly constrained space, so the region of the fastest flow occurs further downstream.

To assess the effect of the particle size, the same long tumbler was simulated using larger particles ($d=3$ mm). Figure 11 shows contours of the streamwise velocity on two representative planes. The two regions of high streamwise velocity still occur for the system with larger particles. Deep in the flowing layer, the streamwise positions of these two regions shift upstream and away from the endwalls, though not to the same extent as with the smaller particles, perhaps

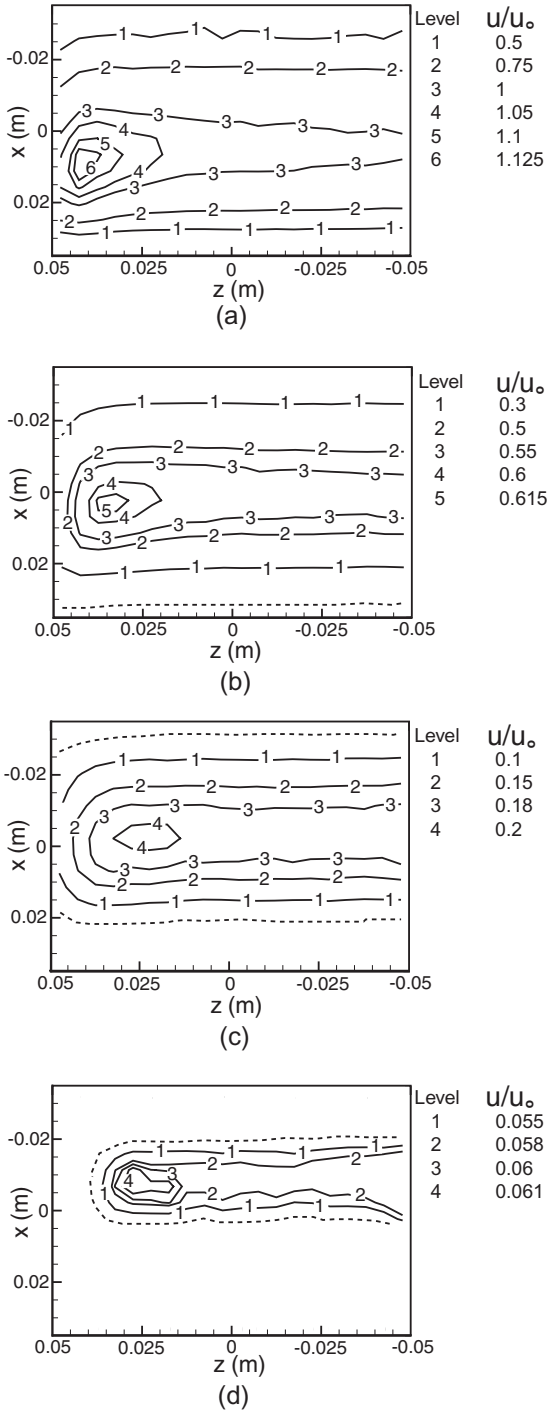

FIG. 8. Contours of streamwise velocity at different depths in the long tumbler of $L=0.10$ m ($L/D=1.43$) with a frictionless endwall at $z=-0.05$ m for 1.5 mm particles. The high velocity region is associated with the frictional left endwall from the surface (a) to deep in the layer (d): (a) $y=0$ m; (b) $y=-0.006$ m; (c) $y=-0.012$ m; (d) $y=-0.017$ m. The dashed contour indicates the edge of the flowing layer at the depth indicated. Flow is from top to bottom.

due to the difference in the rheology of the flow for the different particle sizes.

To better show the nature of the velocity field, the streamwise velocity profiles in the axial direction and streamwise

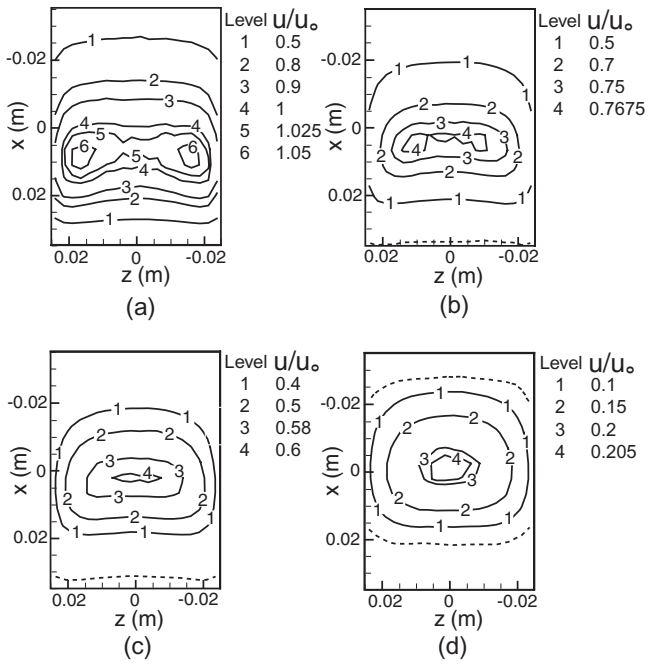

FIG. 9. Contours of streamwise velocity at different depths in the short tumbler of $L=0.05$ m ($L/D=0.71$) for 1.5 mm particles show how the high velocity regions shift upstream and merge from the surface (a) to deep in the layer (d): (a) $y=0$ m; (b) $y=-0.004$ m; (c) $y=-0.006$ m; (d) $y=-0.012$ m. The dashed contour indicates the edge of the flowing layer at the depth indicated. Flow is from top to bottom.

direction for different depths are shown in Fig. 12. Again, the velocities are normalized with the streamwise surface velocity at the center of the tumbler. From Fig. 12(a) it is evident that the two regions of higher streamwise velocity appear at all depths, even near the bottom of the flowing layer at $y=-0.017$ m, though the magnitude is very small. In addition, the axial positions of the two high velocity regions move closer to the center of the tumbler deeper in the flowing layer. The width of the two regions also increases with depth. From Fig. 12(b), it is clear that the maximum in the streamwise velocity shifts so that it occurs downstream of

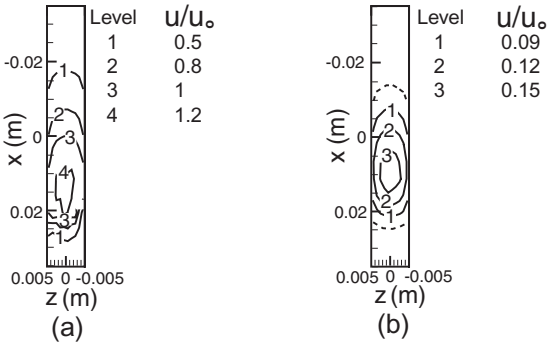

FIG. 10. Contours of streamwise velocity at different depths in the quasi-2D tumbler of $L=0.01$ m ($L/D=0.14$) for 1.5 mm particles have a single high velocity region: (a) $y=0$ m; (b) $y=-0.012$ m. The dashed contour indicates the edge of the flowing layer at the depth indicated. Flow is from top to bottom.

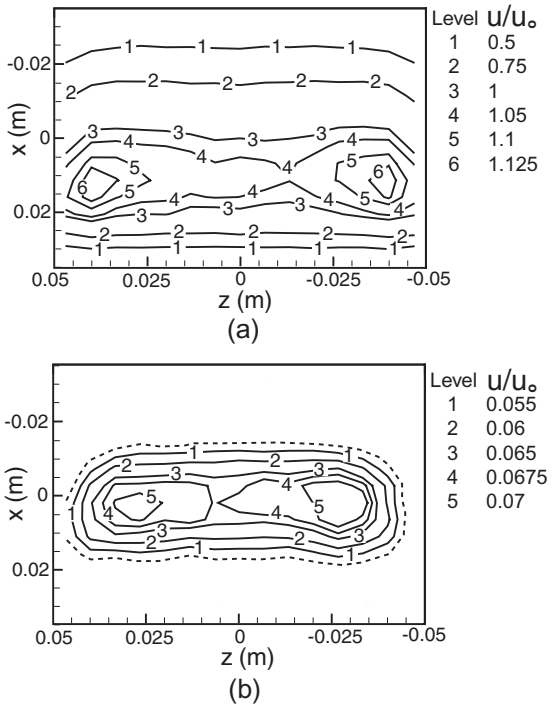

FIG. 11. Contours of normalized streamwise velocity at different depths in the long tumbler of $L=0.10$ m ($L/D=1.43$) for larger 3 mm particles: (a) $y=0$ m; (b) $y=-0.018$ m. The dashed contour indicates the edge of the flowing layer at the depth indicated. Flow is from top to bottom.

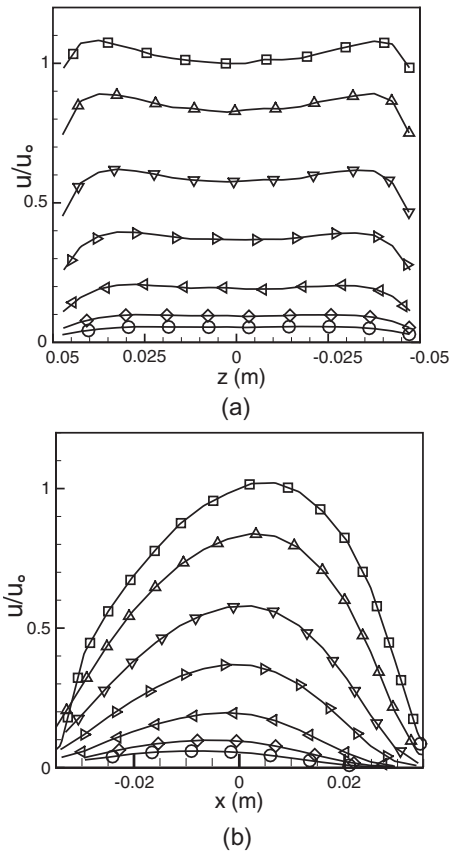

FIG. 12. Normalized streamwise velocity u/u_0 profiles at different depths in the long tumbler ($L=0.10$ m, $L/D=1.43$) for 1.5 mm particles. (a) at $x=0$ m; (b) at $z=0$ m: $y=0$ m (□); $y=-0.003$ m (△); $y=-0.006$ m (▽); $y=-0.009$ m (▷); $y=-0.012$ m (◁); $y=-0.015$ m (◇); $y=-0.017$ m (○).

the midlength of the tumbler in the upper part of the flowing layer and further upstream deeper in the layer.

C. Velocity fluctuations beneath the visible free surface

The multiple interactions of particles in a flowing granular layer result in velocity fluctuations that characterize the diffusion and dissipation in the flow. "Granular temperature" has been used as a term for these fluctuations, due to the analogy with the motion of molecules in a gas. Thus, if the instantaneous velocity of granular particles is $\mathbf{v}=(u,v,w)$ and angled brackets represent the time average, then the granular temperature is defined as $T=\langle \mathbf{v}^2\rangle-\langle \mathbf{v}\rangle^2=u_{\mathrm{rms}}^2+v_{\mathrm{rms}}^2+w_{\mathrm{rms}}^2$ [5]. However, the concept of "temperature" is not as useful for a dissipative granular system as it is in a nondissipative gas. We prefer to consider the random velocity fluctuations in terms of the root-mean-square (rms) values (u_{rms}, v_{rms} and w_{rms}), analogous to the turbulence intensity in fluid systems, which, similar to granular systems, are dissipative. This approach also provides a useful measure of the magnitude of the fluctuations in each of the three component directions. The total velocity fluctuations can be calculated as $V_{\mathrm{total,rms}}=\sqrt{\langle \mathbf{v}^2\rangle-\langle \mathbf{v}\rangle^2}=\sqrt{u_{\mathrm{rms}}^2+v_{\mathrm{rms}}^2+w_{\mathrm{rms}}^2}$.

In Fig. 13 the spanwise profiles of the total and individual components of velocity fluctuations at the free surface normalized by the streamwise surface velocity at the center of the tumbler, u_0, are plotted for the three tumblers. The velocity fluctuations for all three components of velocity generally increase near the endwalls, while the fluctuations are smallest near the axial center of the tumbler. Moreover, the transverse and axial fluctuations are always similar in magnitude and both are smaller than the streamwise fluctuations. The lateral confinement of the endwalls reduces the axial velocity fluctuations, w_{rms}, immediately adjacent to the endwalls for the short tumbler and the long tumbler. (A denser mesh of bins near the endwalls to increase resolution in the long tumbler is necessary to adequately resolve the fluctuations.) For the quasi-2D tumbler, fluctuations in all three velocity components drop immediately adjacent to the endwalls so that the total velocity fluctuation, $V_{\mathrm{total,rms}}$, decreases near endwalls rather than increasing as it does in the long and short tumblers.

The normalized fluctuations along the streamwise direction for the three tumblers are shown in Fig. 14. The tumbler length has little effect on the general nature of the velocity fluctuations in the streamwise direction. In all cases, except for very near the downstream end of the flowing layer, the surface velocity fluctuations grow monotonically along the length of the flowing layer, even after the mean streamwise velocity decreases after the midlength of the flowing layer [Fig. 12(b)]. This is consistent with MRI measurements [30], although the diffusion coefficient was measured rather than the velocity fluctuations. Thus, near the downstream end of the flowing layer the velocity fluctuations may be larger than

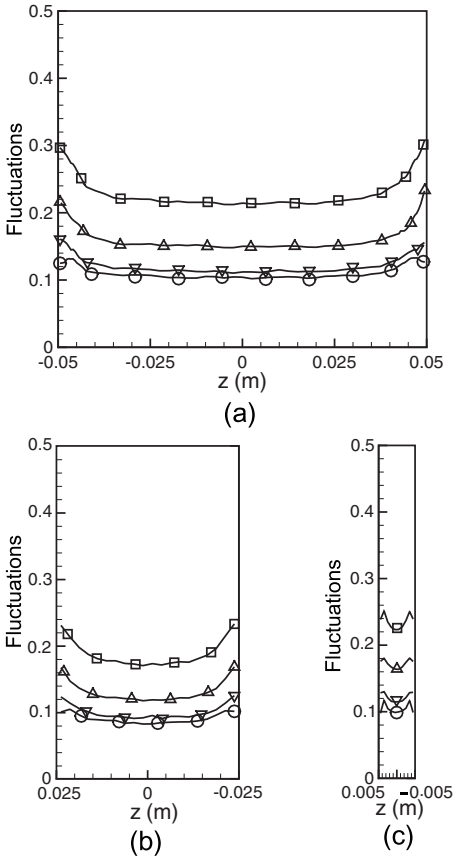

FIG. 13. Normalized velocity fluctuations on the free surface ($y=0$ m) at $x=0$ m, along the length of the three tumblers for 1.5 mm particles. (a) $L=0.10$ m ($L/D=1.43$); (b) $L=0.05$ m ($L/D=0.71$); (c) $L=0.01$ m ($L/D=0.14$). Symbols: $V_{\text{total,rms}}/u_0$ (□); u_{rms}/u_0 (△); v_{rms}/u_0 (▽); w_{rms}/u_0 (○).

the local average velocity. For the long tumbler and the short tumbler the fluctuations grow rapidly at first at the upstream end of the flowing layer as the flow is initiated, then increase more slowly in the middle portion of the flowing layer followed by more rapid growth again in the downstream portion approaching a maximum near the end of the flowing layer. In the quasi-2D case, the velocity fluctuations grow somewhat more quickly along most of the length of the flowing layer than for the long and short tumblers, with an increased growth rate near the end of the flowing layer. Again, in all cases the streamwise velocity fluctuations are larger than the transverse and axial fluctuations, which are similar in magnitude.

To understand the variation of the velocity fluctuations with the depth as well as the endwall effects, the normalized components of the velocity fluctuations are plotted in Fig. 15 for the long tumbler at the midlength of flowing layer, $x=0$ m, at two representative positions: the axial center of the tumbler, $z=0$ m, and near the endwall at $z=-0.0475$ m. The velocity fluctuations increase moving from deep in the layer toward the surface. In the upper portion of the flowing layer, the magnitudes of all fluctuations near the endwalls are larger than their counterparts at the center, probably because the particles are rebounding off the endwall and have substantial room for motion. At the free surface, the velocity

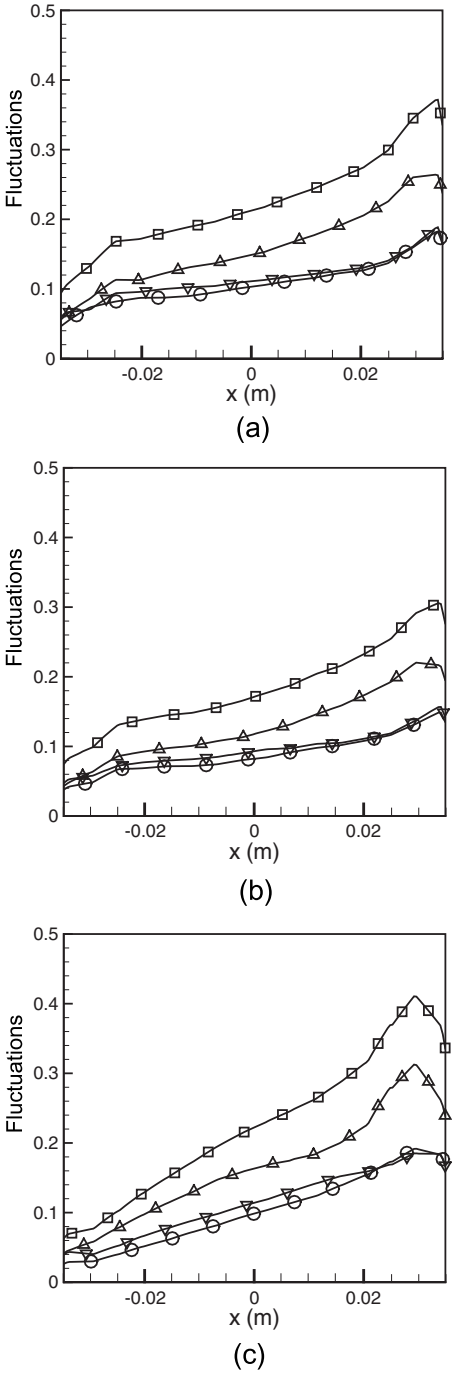

FIG. 14. Normalized velocity fluctuations on the free surface at $z=0$ m along the streamwise direction of three tumblers for 1.5 mm particles generally increase from the beginning to the end of the flowing layer. (a) $L=0.10$ m ($L/D=1.43$); (b) $L=0.05$ m ($L/D=0.71$); (c) $L=0.01$ m ($L/D=0.14$). Symbols: $V_{\text{total,rms}}/u_0$ (□); u_{rms}/u_0 (△); v_{rms}/u_0 (▽); w_{rms}/u_0 (○). Flow is from left to right.

fluctuations are reduced, since particle collisions occur less frequently as a result of the low number density of particles. Deeper in the flowing layer the fluctuations at the endwalls are less than those near the center due to the confinement from lateral endwalls and other particles deep in the layer. Surprisingly, detectable velocity fluctuations occur even in the "fixed bed," although they are quite small (only about 3%

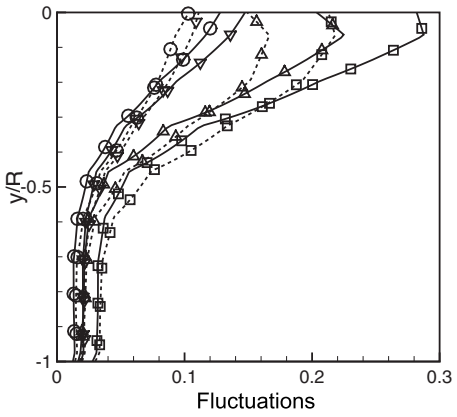

FIG. 15. Comparison of profiles of the normalized velocity fluctuations along the depth at $x=0$ m in the long tumbler ($L=0.10$ m, $L/D=1.43$) for 1.5 mm particles: at the center of tumbler (dashed curves, $z=0$ m) and near the endwall at a location of $z=-0.0475$ m (solid curves). Symbols: $V_{\text{total,rms}}/u_0$ (□); u_{rms}/u_0 (△) v_{rms}/u_0 (▽); w_{rms}/u_0 (○).

of u_0). These fluctuations arise from rearrangements of particles as the gravity vector changes orientation with respect to the fixed bed as the tumbler rotates.

D. Axial velocity in the tumbler

Recent measurements of the velocity on the surface of the flowing layer by Pohlman *et al.* [12] have shown that boundary effects introduce axial flow near the endwalls in long tumblers, as indicated by the curved streamtraces at the surface of the flowing layer in Fig. 3. The axial velocity is relatively small—only about $O(0.1)$ of the streamwise surface velocity at most [12]—but may be significant with respect to transport of material near the endwalls [14].

As shown in the contour plots of axial velocity for the free surface in the long tumbler in Fig. 16(a), the simulation captures the general character of the axial flow that has been previously explored in experiments [12]: the axial flow near the endwalls is toward the center of the tumbler in the upstream portion of the flowing layer and toward the endwalls in the downstream portion; the magnitude of axial velocity at downstream portion is larger than that of upstream portion; and the whole axial flow is roughly symmetric about the axial center of the tumbler, but not symmetric about the midlength of the flowing layer. The axial velocity comes about from the combined effects of endwall friction and mass conservation [12,13]. Mass conservation requires that all the particles in the fixed bed in any slice of the tumbler must flow through the flowing layer once every half revolution for a half-filled tumbler. Particles in the slices nearest the endwalls are slowed by endwall friction. Since the flowing layer is thinner near the endwalls (Figs. 5 and 6) and the streamwise velocity is reduced [Fig. 12(a)], the only possibility to conserve mass is for the particles to flow axially away from the endwall in the upstream portion of the flowing layer to reach a faster streamwise flow (Fig. 7) and then move back toward the endwall in the downstream portion of the flowing layer resulting in the situation shown in Fig. 16(a).

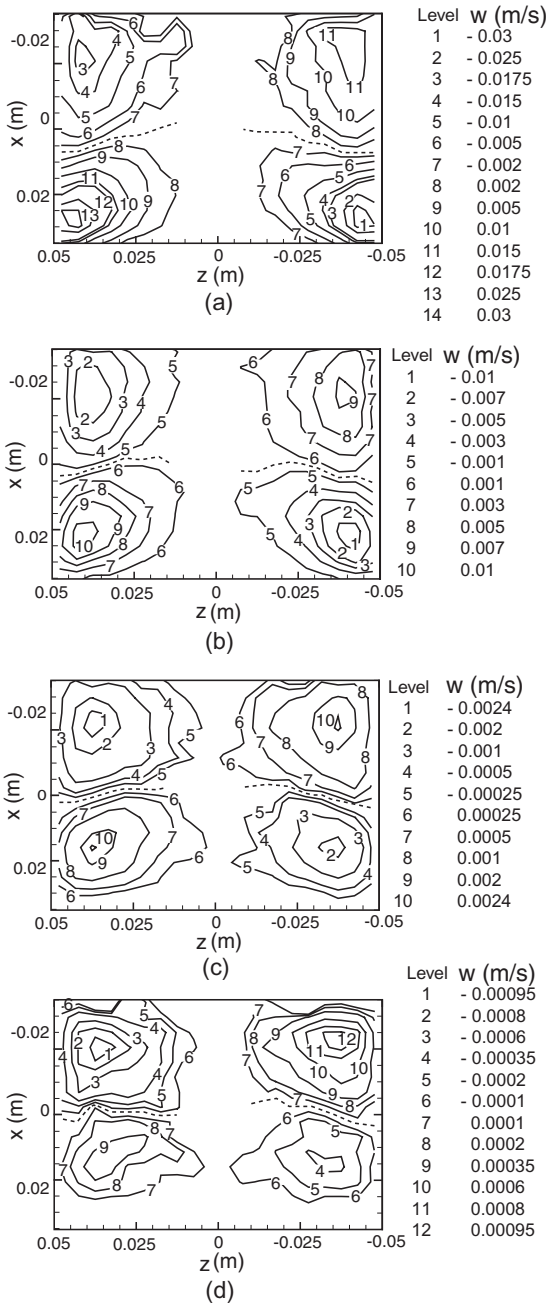

FIG. 16. The axial flow fields at different depths in the long tumbler ($L=0.10$ m, $L/D=1.43$) for 1.5 mm particles show that the axial flow is retained at all depths: (a) at $y=0$ m, (b) at $y=-0.006$ m, (c) at $y=-0.0012$ m, (d) at $y=-0.0017$ m. Flow is from top to bottom.

However, unlike previous experiments, our numerical simulations allow probing the situation below the surface of the flowing layer as shown in Figs. 16(b)–16(d). It is quite clear that the axial flow persists deep into the flowing layer, though the magnitude of the axial velocity diminishes, as would be expected. The magnitude of the velocity in the upstream portion is less than in the downstream portion in the upper part of the flowing layer [Figs. 16(a) and 16(b)], but larger deep in the flowing layer [Fig. 16(d)]. Moving from the free surface to deep in the layer, the region with

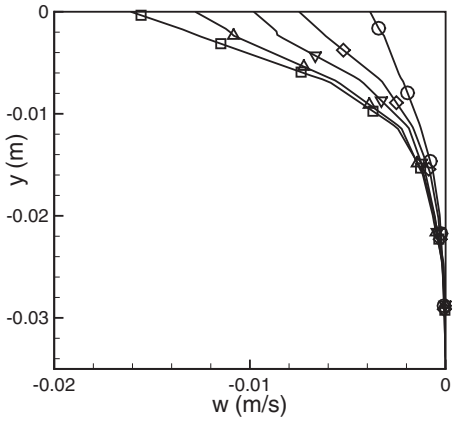

FIG. 17. Profile of the axial velocity along the y direction at different axial positions at $x=-0.02$ m in the long tumbler ($L=0.10$ m, $L/D=1.43$) for 1.5 mm particles. Symbols: $z=0.04$ m (□); $z=0.035$ m (△); $z=0.03$ m (▽); $z=0.025$ m (◇); $z=0.02$ m (○).

axial flow does not vary much in size, but the location of the maximum axial velocity moves further from the endwall and slightly toward the axis of rotation, particularly for the downstream portion. At all depths, the interfaces between upstream and downstream portions (dashed curves) are skewed slightly upstream from the endwalls inward. These curves move upstream with increasing the depth in the flowing layer.

It is helpful to consider the depthwise profile of axial velocity. In Fig. 17, the axial velocity at $x=-0.02$ m, near where maximum axial velocity occurs, is shown for different axial positions. Since this is the upstream portion of the flowing layer, the axial velocity is directed away from the left endwall ($w<0$) for portions in the left half of the tumbler ($z>0$). It is clear that the axial velocity extends deep into the flowing layer. The axial velocity has a nearly linear profile in the upper portion of the flowing layer with a smooth transition to the fixed bed.

The effect of the endwalls on the granular system has two components: the lateral confinement through collisions between endwalls and particles, and the tangential frictional force between endwalls and particles from which the axial flow arises due to mass conservation. Therefore, the axial flow associated with the two endwalls should be independent of each other for a long enough tumbler. In fact, Pohlman *et al.* [12] indicated that for $L/D>1$, the effects of the endwalls do not interact with one another. To confirm this, the axial flow of the long tumbler ($L=0.10$ m, $L/D=1.43$) is compared with two other cases: the same tumbler but with one frictionless endwall at $z=-0.05$ m (lateral confinement only) and a longer tumbler, $L=0.15$ m ($L/D=2.14$). The axial velocity profiles of these three cases are compared quantitatively along the axial (z), streamwise (x), and transverse (y) direction in Figs. 18–20. In Fig. 18, the patterns of axial velocity profiles on the free surface at the frictional end of three cases are comparable, though the pattern is necessarily shifted for the $L=0.15$ m case. The axial velocity at the frictionless endwall is negligible, confirming that the axial velocity arises solely due to friction at the endwall not lateral confinement.

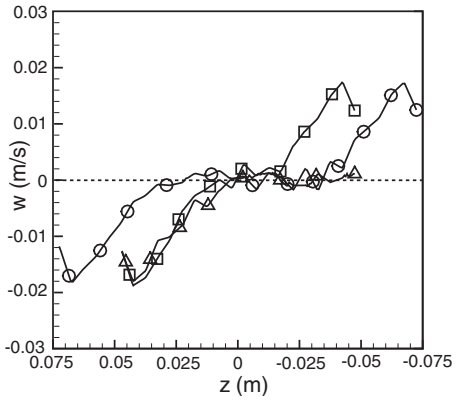

FIG. 18. The free surface axial velocity at $x=-0.02$ m along the axial direction for 1.5 mm particles matches near the frictional endwalls regardless of the tumbler length: □, $L=0.10$ m ($L/D=1.43$), both endwalls are frictional; ○, $L=0.15$ m ($L/D=2.14$), both endwalls are frictional; △, $L=0.10$ m ($L/D=1.43$) with a frictionless end wall at $z=-0.05$ m.

Figure 19 illustrates that the axial velocity profiles along the streamwise direction at the free surface a short distance from the frictional endwall are not affected by the length of the tumbler or the frictionless endwall. Likewise, profiles of the axial velocity through the depth of the flowing layer (Fig. 20) collapse almost perfectly. These results indicate that the axial flow near the two endwall regions results solely from the friction interaction between the endwalls and the particles (not particle exclusion at the endwalls) and that the effect penetrates through the depth of the flowing layer. Furthermore, these results are consistent with experiments measuring the axial surface velocity [12] that indicate these endwall flows are independent of each other and independent of the tumbler length for long tumblers.

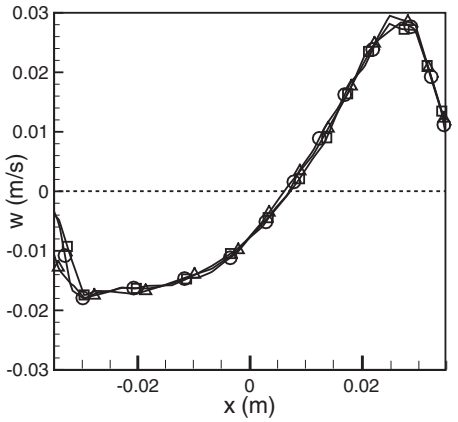

FIG. 19. Free surface axial velocity 0.01 m from the frictional endwall [$z=0.04$ m for two $L=0.10$ m ($L/D=1.43$) tumblers and $z=0.065$ m for $L=0.15$ m ($L/D=2.14$) tumbler] along the streamwise direction for 1.5 mm particles match, regardless of the tumbler length: □, $L=0.10$ m ($L/D=1.43$), both endwalls are frictional; ○, $L=0.15$ m ($L/D=2.14$), both endwalls are frictional; △, $L=0.10$ m ($L/D=1.43$) with a frictionless endwall at $z=-0.05$ m.

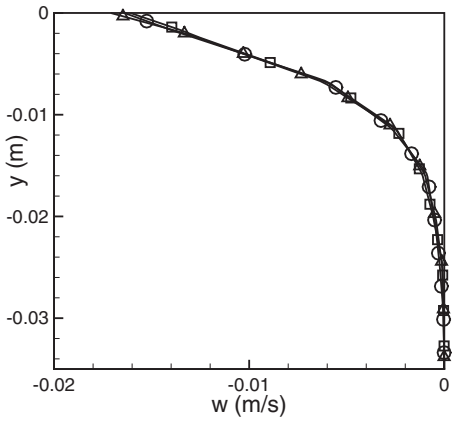

FIG. 20. Axial velocity profile with depth at $x=-0.02$ and 0.01 m away from the frictional endwall for three cases with 1.5 mm particles match, regardless of the tumbler length: □, $L=0.10$ m ($L/D=1.43$), both endwalls are frictional; ○, $L=0.15$ m ($L/D=2.14$), both endwalls are frictional; △, $L=0.10$ m ($L/D=1.43$) with a frictionless endwall at $z=-0.05$ m.

IV. CONCLUSIONS

Endwalls play a major role in the structure and velocity field in the flowing layer of a cylindrical tumbler. When the endwalls are far enough apart, approximately one tumbler diameter (D) or more from each other, independent regions of altered flow occur proximal to the endwalls throughout the depth of the flowing layer, consistent with the measurements at the surface [12]. The friction at the endwalls slows the particles that are immediately adjacent so that (1) the flowing layer is not as deep as further from the endwalls and (2) the streamwise velocity of the particles is slower immediately adjacent to the endwalls than further from the endwalls. This sets up a situation in which a short distance from the endwalls, within one tumbler radius R from an endwall, the flow adjusts to accommodate mass conservation. Specifically, an axial velocity field is set up to carry particles to a faster flowing region a short distance from the endwall. Not only is the streamwise flow faster in this region than it is near the endwalls, it is faster than the flow far from the endwalls at the center of the tumbler. The flowing layer deepens to further accommodate the particles moving into the region from next to the endwalls.

Simulations with longer tumblers or tumblers with one frictionless endwall clearly indicate that this phenomenon is a direct result of endwall friction and that it extends less than one tumbler radius from the endwall. When frictional endwalls are closer that $2R$, these regions of faster flow merge partially (for the short tumbler) or completely (for the quasi-2D tumbler). Likewise, the regions in which the flowing layer is deeper merge as the endwalls get closer to one another. While recent experiments provide similar results with regard to the extent of the region near the endwalls where the streamwise velocity is higher and speculate that this is a result of the impact of endwall friction on mass conservation [12–14], these studies were limited to surface velocity measurements. These DEM simulations make it clear that the axial flow and accelerated streamwise flow in the region near the endwalls not only extend through the depth of the flowing layer, but also alter the depth of the flowing layer locally. Furthermore, these previous studies could only speculate on the cause of this phenomenon, though in one case it was shown that higher friction at an endwall (using sandpaper) accentuated the axial and streamwise flow measured at the surface [12]. These DEM simulations with a frictionless endwall show that the axial flow, higher streamwise velocity, and deeper flowing layer typically associated with a frictional endwall are absent altogether when the endwall is frictionless.

In spite of this better understanding of the detailed flow of monodisperse particles through the depth of the flowing layer, questions still abound. Specifically, how the frictional endwalls affect the mixing and segregation of bidisperse particles, particularly in terms of radial segregation and pattern forming in quasi-2D bidisperse systems and in terms of axial banding in long tumbler, remains an open question. Likewise, the impact of frictional interactions between particles and walls for curved walls is not clear. For instance, it is unclear if friction can cause an axial flow in spherical tumblers. Nevertheless, further experiments and simulations can shed light on these and other issues, particularly now that it is possible to simulate large numbers of particles using reasonably low cost computers.

ACKNOWLEDGMENTS

This work was funded by Northwestern University and Office of Basic Energy Sciences of the Department of Energy Grant No. DE-FG02-95ER14534.

[1] GDR MiDi, Eur. Phys. J. E **14**, 341 (2004).
[2] J. M. Ottino and D. V. Khakhar, Annu. Rev. Fluid Mech. **32**, 55 (2000).
[3] S. W. Meier, R. M. Lueptow, and J. M. Ottino, Adv. Phys. **56**, 757 (2007).
[4] A. V. Orpe and D. V. Khakhar, Phys. Rev. Lett. **93**, 068001 (2004).
[5] N. Jain, J. M. Ottino, and R. M. Lueptow, Phys. Fluids **14**, 572 (2002).
[6] A. V. Orpe and D. V. Khakhar, J. Fluid Mech. **571**, 1 (2007).
[7] E. Clement, J. Rajchenbach, and J. Duran, Europhys. Lett. **30**, 7 (1995).
[8] F. Cantelaube, D. Bideau, and S. Roux, Powder Technol. **93**, 1 (1997).
[9] G. H. Ristow, Europhys. Lett. **34**, 263 (1996).
[10] T. S. Komatsu, S. Inagaki, N. Nakagawa, and S. Nasuno, Phys. Rev. Lett. **86**, 1757 (2001).
[11] J. E. Maneval, K. M. Hill, B. E. Smith, A. Caprihan, and E.

Fukushima, Granular Matter **7**, 199 (2005).
[12] N. A. Pohlman, J. M. Ottino, and R. M. Lueptow, Phys. Rev. E **74**, 031305 (2006).
[13] N. A. Pohlman, S. W. Meier, R. M. Lueptow, and J. M. Ottino, J. Fluid Mech. **560**, 355 (2006).
[14] A. Santomaso, M. Olivi, and P. Canu, Chem. Eng. Sci. **59**, 3269 (2004).
[15] J. Bridgwater, N. W. Sharpe, and D. C. Stocker, Trans. Inst. Chem. Eng. **47**, T114 (1969).
[16] K. M. Hill and J. Kakalios, Phys. Rev. E **49**, R3610 (1994).
[17] S. J. Fiedor and J. M. Ottino, Phys. Rev. Lett. **91**, 244301 (2003).
[18] A. A. Boateng and P. V. Barr, J. Fluid Mech. **330**, 223 (1997).
[19] D. J. Parker, A. E. Dijkstra, T. W. Martin, and J. P. K. Seville, Chem. Eng. Sci. **52**, 2011 (1997).
[20] M. Nakagawa, S. A. Altobelli, A. Caprihan, E. Fukushima, and E. K. Jeong, Exp. Fluids **16**, 54 (1993).
[21] E. Fukushima, Annu. Rev. Fluid Mech. **31**, 95 (1999).
[22] P. A. Cundall and D. L. Stack, Geotechnique **29**, 47 (1979).
[23] G. H. Ristow, *Pattern Formation in Granular Materials* (Springer, Berlin, 2000).
[24] J. Schafer, S. Dippel, and D. E. Wolf, J. Phys. I **6**, 5 (1996).
[25] D. C. Rapaport, Phys. Rev. E **65**, 061306 (2002).
[26] M. P. Allen and D. J. Tildesley, *Computer Simulation of Liquids* (Oxford University Press, Oxford, 2000).
[27] C. M. Dury and G. H. Ristow, J. Phys. I **7**, 737 (1997).
[28] C. M. Dury, G. H. Ristow, J. L. Moss, and M. Nakagawa, Phys. Rev. E **57**, 4491 (1998).
[29] B. A. Socie, P. Umbanhowar, R. M. Lueptow, N. Jain, and J. M. Ottino, Phys. Rev. E **71**, 031304 (2005).
[30] A. Caprihan and J. D. Seymour, J. Magn. Reson. **144**, 96 (2000).